Mechatronics 104 (2024) 103265

Contents lists available at ScienceDirect

Mechatronics

journal homepage: www.elsevier.com/locate/mechatronics

Stiffness-fault-tolerant control strategy for elastic actuators with interaction impedance adaptation ☆

Rodrigo J. Velasco-Guillen [a,*], Raphaël Furnémont [b], Tom Verstraten [b], Bram Vanderborght [b,c], Josep M. Font-Llagunes [d,e], Philipp Beckerle [a,f]

[a] Chair of Autonomous Systems and Mechatronics (ASM), Friedrich-Alexander-Universität (FAU) Erlangen-Nürnberg, Erlangen, Germany
[b] Robotics and MultiBody Mechanics Research Group, Vrije Universiteit Brussel (VUB), Brussels, Belgium
[c] Interuniversity Microelectronics Centre (IMEC), Belgium
[d] Biomechanical Engineering Lab, Dept. of Mechanical Engineering and Research Centre for Biomedical Engineering, Universitat Politècnica de Catalunya (UPC), Barcelona, Spain
[e] Institut de Recerca Sant Joan de Déu, Esplugues de Llobregat, Spain
[f] Dept. Artificial Intelligence in Biomedical Engineering (AIBE), Friedrich-Alexander-Universität (FAU) Erlangen-Nürnberg, Erlangen, Germany

ARTICLE INFO

Keywords:
Elastic actuation
Fault-tolerance
Impedance control
Online parameter estimation
Human–robot interaction

ABSTRACT

Elastic actuators have the potential to enable safe interaction and energy efficient mobility, making them suitable for physical human–robot interaction. However, their increased complexity makes technical faults and their prevention a relevant research topic, particularly considering faults in elastic and kinematic elements. In this article we investigate a stiffness-fault-tolerant control strategy for elastic actuators, based on impedance control, which compensates for internal faults and adapts to a desired interaction impedance behavior. We analyze the control strategy regarding its stability, and adapt it to the dynamic characteristics of two systems: a mechanically adjustable compliance actuator (MACCEPA) and a series–parallel elastic actuator (+SPEA), highlighting the strategy's general applicability to multiple actuator designs, considering nonlinear and redundant characteristics. Experimental validation with these systems shows that the control strategy is capable of accurately tracking reference output trajectories and adapting interaction characteristics, under fault and disturbance conditions, showcasing the versatile applicability of the strategy while achieving fault-tolerance.

1. Introduction

Fault-tolerant control can be achieved through algorithms that detect and adapt to changes in the behavior of a system such that it continues to operate nominally [1]. This type of fault management strategy is particularly important to ensure safety and system dependability [2]. Fault tolerance in mechatronic systems is often handled by robust control strategies that can circumvent unknown disturbances, uncertain parameterization, or deviations from nominal operation [3–7]. Moreover, impedance control can be used to regulate the dynamic interaction between a robot and its environment by virtually changing its output impedance [8]. In physical human–robot interaction (pHRI) applications, it can be used to improve the interaction experience by modulating the dynamic relationship between forces and positions [9]. The combination of impedance control with adaptive and robust control methods has the potential of improving safety and reliability in wearable robotic systems without sacrificing control stability or accuracy in the face of uncertainties and disturbances [10–13].

Elastic or compliant actuators have been of particular interest in the design of wearable robots, such as prostheses and exoskeletons, due to their potential for inherently safer human–robot interaction and energy efficiency [14]. The most common topology for these types of actuators is probably the series elastic actuator (SEA), where an elastic element couples the inertia of the output and the actuated input. The elastic element allows energy storage and could potentially improve safety by adding output backdrivability through elastic deformation [15]. The parallel elastic actuator (PEA) topology couples the output and input rigidly and adds an elastic element in parallel to the actuated input. The elastic element, in this case, limits the motion of the output but adds a passive torque that can benefit energy efficiency in tasks with relevant static loads [15]. Series–parallel elastic actuators (SPEA) combine the two aforementioned topologies by adding multiple SEA units in parallel to a single output, which creates an over-actuated system that can lower the required nominal motor torques [16].

☆ This paper was recommended for publication by Associate Editor Takeshi Hatanaka.

* Corresponding author.
E-mail address: rodrigo.velasco@fau.de (R.J. Velasco-Guillen).

https://doi.org/10.1016/j.mechatronics.2024.103265
Received 29 January 2024; Received in revised form 23 September 2024; Accepted 12 October 2024
Available online 28 October 2024

Variable impedance actuators (VIA) modify their inherent mechanical impedance through various kinds of mechanisms that may introduce nonlinear functions [17]. Yet, due to their higher system complexity and increased control requirements, when compared to rigid actuators, investigating faults in VIAs holds practical relevance [18]. These actuators often include kinematic elements, such as linkages and cables, that are prone to failing [18]. Furthermore, the material of an elastic element under cyclic loading can experience microscopic damages, due to fatigue or overloading, which lowers the effective stiffness of the element [19]. These faults might change the elastic behavior of the actuator and make it necessary to implement a reconfiguration system to prevent failures through analytically redundant components [20] that compensate for the stiffness fault to maintain the desired system operation until the faulty element can be repaired or replaced. Detecting stiffness faults, particularly when dealing with nonlinear or time-varying stiffness characteristics, can be realized by using online parameter estimation of stiffness characteristics [21–24]. Flacco and De Luca [21] successfully combined a nonlinear stiffness estimator with closed-loop control and showed the practical feasibility of the approach. Moreover, when dealing with elastic materials, monitoring stiffness characteristics online can also be used to evaluate fault severity and predict a possible failure [25].

This article extends previous research on fault-tolerant pHRI in elastic actuators [25–27], where a control strategy based on the passivity-based impedance controller from [28] was implemented. The control strategy was capable of adapting a desired interaction impedance behavior, while detecting and compensating faults in elastic elements using online stiffness estimation. In this article we develop a general method and analyze its stability. We highlight the transferability of the proposed strategy to different elastic actuator topologies and designs, and validate it using two actuators: a mechanically adjustable compliance and controllable equilibrium position actuator (MACCEPA), previously investigated in [26], with non-linear stiffness characteristics; and the redundantly actuated +SPEA, previously simulated in [27], with a rigidly coupled actuation unit and multiple SEA units connected in parallel. The hardware redundancy of the +SPEA already has the potential for fault tolerance by ensuring the continuation of the system should one actuation unit were to fail, and when combined with analytical redundancy methods introduced by fault-tolerant control, its reliability can be improved. The main contributions and research objectives of the article are the following:

1. We propose a fault-tolerant strategy for motion tracking on elastic actuators, demonstrating locally stable dynamics for SEA and PEA topologies. The strategy utilizes impedance control and a stiffness adaptation law to regulate closed-loop dynamics between user interaction torque and trajectory deviation.
2. We experimentally validate the strategy, demonstrating its effectiveness in handling nonlinear stiffness characteristics and integrating control allocation algorithms for redundant actuation, showing robustness to small model mismatches.
3. The general applicability of the control strategy to achieve fault tolerance and stiffness modulation in multiple elastic actuator topologies considering nonlinear and redundant characteristics makes the control approach a valid compliant control candidate for pHRI applications.

In literature, adaptive and robust control methods are an alternative to achieve fault-tolerance in elastic actuators by implementing closed loop control without requiring full knowledge of the model. Many control schemes compensate for uncertain parameters and disturbances by applying control stabilization algorithms [29,30] or disturbance observers [31,32]. However, the stability of these methods cannot always be guaranteed for the large magnitudes of parameter uncertainties which might be found in a faulty system. Our fault-tolerant control approach for elastic actuators relies instead on online estimation of time-varying stiffness parameters to reconfigure the control law, a concept similar to adaptive control strategies that rely on the estimation of unknown parameters [33–35]. However, many of these approaches are limited to a linear SEA topology and do not consider the causes nor impact of changes in parameters, e.g., faults. Our approach for trajectory tracking considers that parameters such as inertia and friction coefficients can be known with sufficient certainty and only parameters related to faulty elements need to be estimated. Furthermore, our approach is also extended to multiple elastic actuator topologies and handles nonlinear stiffness and redundant characteristics.

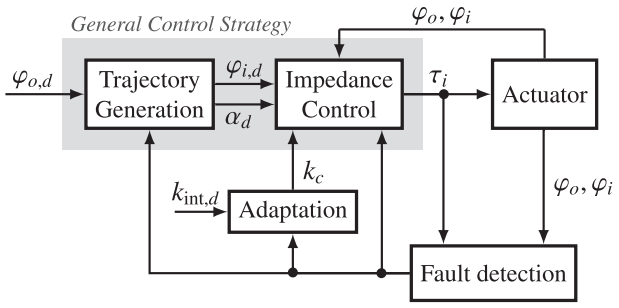

Fig. 1. Stiffness-fault-tolerant control strategy. A passivity-based impedance controller, combined with a trajectory generation algorithm, allows to virtually adapt the interaction impedance between the actuator and its environment, modulating the allowed deviation of output position φ_o from a reference trajectory $\varphi_{o,d}$. A fault detection algorithm observes uncertain model parameters related to elastic behavior to correct control calculations and compensate for fault occurrences.

The rest of the article is organized as follows. Section 2 details the general control strategy. Section 3 exemplifies how the strategy is implemented for different actuator topologies and analyzes its stability. Section 4 describes the MACCEPA and +SPEA setups and provides detailed description of their dynamic characteristics. Section 5 evaluates dynamic motion experiments conducted on the two actuators. Finally, Section 6 concludes on the versatile applicability of the control algorithm and outlines future work.

2. Control strategy

The control strategy is shown in Fig. 1. Consider an elastic actuator with input position φ_i at the motor side and output position φ_o at the load side. A motor unit exerts an input torque τ_i and an elastic element exerts a torque τ_s, which is a function of its deformation α, i.e., $\tau_s = f_s(\alpha)$. The general objective of the control strategy is to track a reference output trajectory $\varphi_{o,d}$ by generating a desired input trajectory $\varphi_{i,d}$ and elastic deflection α_d which compensate for output dynamics. An impedance controller is then used to provide an input torque and thereby track the input and deformation references. A fault detection algorithm observes relevant parameters related to the elastic properties of the actuator and feeds them back to the controller to perform the appropriate calculations. If a fault occurs, the value of the observed parameters will deviate from the expected values and will be propagated through the controller calculations to correct the system behavior.

2.1. Impedance controller

A passivity-based impedance controller tracks a desired trajectory $\varphi_{i,d}$ as if virtual spring and damper elements act on the present trajectory φ_i to attain an equilibrium position at $\varphi_i = \varphi_{i,d}$ and $\dot{\varphi}_i = \dot{\varphi}_{i,d}$. In an elastic actuator this can be achieved by defining a control law that yields the desired system behavior while performing feedback compensation of undesired terms:

$$\tau_i = \frac{J_i}{J_{i,d}} u + \left(1 - \frac{J_i}{J_{i,d}}\right) \tau_c + \tau_{\text{fric,i}} + \tau_{\text{comp},i}, \tag{1}$$

where J_i denotes the input-side inertia, $J_{i,d}$ is the desired inertia which is to be virtually shaped, τ_c is the coupling torque (external from the input-side), $\tau_{\text{fric,i}}$ is the internal friction compensation term, $\tau_{\text{comp},i}$ is an optional feedback compensation term that compensates for unwanted terms at the input side, while u is a control input, defined by [28], that performs feedforward compensation of inertial and elastic torque, and tracks the reference trajectory:

$$u = J_i\ddot{\varphi}_{i,d} + \tau_{s,d} + k_c(\varphi_{i,d} - \varphi_i) + d_c(\dot{\varphi}_{i,d} - \dot{\varphi}_i)\,, \tag{2}$$

where $\tau_{s,d} = \mathrm{f}_s(\alpha_d)$ denotes the desired elastic torque, while k_c and d_c are virtual stiffness and damping parameters, respectively, that act as a PD-control for the input position.

2.2. Trajectory generation

A secondary objective for the control strategy can be accomplished by manipulating the elastic torque behavior without deviating from the output reference. To do so, the trajectory generation algorithm requires finding $\varphi_{i,d}$ such that the reference output $\varphi_{o,d}$ is achieved, while the elastic torque created from the reference deflection α_d compensates for inertial, gravitational and friction torques at the output:

$$\mathrm{f}_s(\alpha_d) = J_o\ddot{\varphi}_{o,d} + \tau_{g,o} + \tau_{\text{fric},o}\,, \tag{3}$$

where J_o is the output-side inertia, while $\tau_{g,o}$ and $\tau_{\text{fric},o}$ are the output gravitational and friction torques, respectively.

Solving Eq. (3) for α_d analytically may not be possible if $\mathrm{f}_s(\alpha)$ denotes a nonlinear function or if it involves a combination of multiple springs. The particular algorithms for the experimental systems considered in this article are presented in Section 4.3.

The control law in Eq. (1) can be generally applied to any actuator topology, while the trajectory generation algorithm in Eq. (3) can be applied in elastic actuators with multiple degrees of freedom or when variable stiffness mechanisms are present.

3. Actuator dynamics

We will exemplify how the control strategy is applied to two elastic actuator topologies: the series elastic actuator (SEA) and the parallel elastic actuator (PEA). We analyze the impedance behavior of the actuators under closed-loop control. Since $\varphi_{o,d}$ and $\varphi_{i,d}$ act as time-varying virtual equilibrium positions [28], the closed-loop dynamics are defined with respect to the errors $\tilde{\varphi}_o = \varphi_{o,d} - \varphi_o$ and $\tilde{\varphi}_i = \varphi_{i,d} - \varphi_i$. The elastic deflection α is defined for each topology as:

$$\alpha = \begin{cases} \varphi_i - \varphi_o & \text{for SEA,} \\ \varphi_o & \text{for PEA.} \end{cases}\,. \tag{4}$$

Furthermore, we linearize the elastic torque behavior around the deflection α:

$$\mathrm{f}(\alpha_d) - \mathrm{f}(\alpha) \approx k_s\tilde{\alpha}\,, \quad k_s = \frac{\partial \mathrm{f}_s}{\partial \alpha}(\alpha)\,. \tag{5}$$

where $\tilde{\alpha} = \alpha_d - \alpha$ and k_s is the instantaneous stiffness.

3.1. SEA closed-loop dynamics

Consider a general SEA structure whose dynamic equations that describe the motion of the system are the following:

$$J_o\ddot{\varphi}_o - \mathrm{f}_s(\varphi_i - \varphi_o) = -\tau_{\text{fric},o} - \tau_{g,o} - \tau_{\text{int}}\,, \tag{6a}$$

$$J_i\ddot{\varphi}_i + \mathrm{f}_s(\varphi_i - \varphi_o) = \tau_i - \tau_{\text{fric},i}\,, \tag{6b}$$

where τ_{int} denotes torque introduced through user interaction.

Considering Eq. (1) with $\tau_c = \mathrm{f}_s(\varphi_i - \varphi_o)$ and $\tau_{\text{comp},i} = 0$, and combining it with Eqs. (2), (3), (4), (5), and (6), we obtain the following closed-loop dynamics for SEA topologies:

$$\begin{bmatrix} J_o & 0 \\ 0 & J_{i,d} \end{bmatrix}\begin{bmatrix} \ddot{\tilde{\varphi}}_o \\ \ddot{\tilde{\varphi}}_i \end{bmatrix} + \begin{bmatrix} 0 & 0 \\ 0 & d_c \end{bmatrix}\begin{bmatrix} \dot{\tilde{\varphi}}_o \\ \dot{\tilde{\varphi}}_i \end{bmatrix} + \begin{bmatrix} k_s & -k_s \\ -k_s & k_s + k_c \end{bmatrix}\begin{bmatrix} \tilde{\varphi}_o \\ \tilde{\varphi}_i \end{bmatrix} = \begin{bmatrix} \tau_{\text{int}} \\ 0 \end{bmatrix}\,, \tag{7}$$

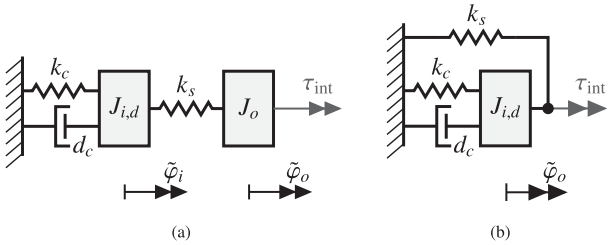

Fig. 2. Characteristic diagram of an impedance controlled elastic actuator for the (a) SEA and (b) PEA topologies.

which corresponds to the dynamics of a linear mechanical system. The characteristic diagram of an impedance-controlled SEA is shown in Fig. 2(a).

3.2. PEA closed-loop dynamics

Consider a general PEA structure where input and output are directly coupled, i.e., $\varphi_i = \varphi_o$, with J_i containing the combined inertia of the load and the reflected inertia of the motor. The dynamic equation that describes the motion of the system is the following:

$$J_i\ddot{\varphi}_o + \mathrm{f}_s(\varphi_o) = \tau_i - \tau_{\text{fric},i} - \tau_{g,o} - \tau_{\text{int}}\,. \tag{8}$$

Considering Eq. (1) with $\tau_c = \mathrm{f}_s(\varphi_o) + \tau_{\text{int}}$ and $\tau_{\text{comp},i} = \tau_{g,o}$ and combining it with Eqs. (2), (4), (5), and (8), we obtain the following closed-loop dynamics for the PEA topology:

$$J_{i,d}\ddot{\tilde{\varphi}}_o + d_c\dot{\tilde{\varphi}}_o + (k_s + k_c)\tilde{\varphi}_o = \tau_{\text{int}}\,, \tag{9}$$

which corresponds to the dynamics of a linear mechanical system. The characteristic diagram of an impedance-controlled PEA is shown in Fig. 2(b).

Note that in this case, due to the direct coupling, the control law alone is enough to achieve the desired system behavior. The trajectory generation algorithm can still be implemented, if the stiffness of the parallel spring can be dynamically varied, to indirectly compensate for part of the system dynamics and potentially lower the motor torque requirements. Note also that inertia shaping, i.e., $J_i \neq J_{i,d}$, requires the direct measurement of τ_{int}. In practice, it might be convenient to consider the method without inertia shaping, i.e., $J_i = J_{i,d}$, which simplifies Eq. (1) and avoids the need of additional torque measurement efforts.

3.3. Stability

The stability analysis of the closed-loop dynamics shown in Eqs. (7) and (9) is conducted by adapting the approach from [28], which considers energy storage functions of the physical passive elements and the virtual spring introduced by control. Therefore, the nonlinear case is considered by proving that the system is locally stable around the reference trajectory. It is assumed that the system performs free motion ($\tau_{\text{int}} = 0$) and singular positions are avoided.

Consider that $T(J,\dot{\varphi}) = \frac{1}{2}J\dot{\varphi}^2$ denotes the kinetic energy storage function of a rotating rigid body with moment of inertia J and speed $\dot{\varphi}$, while $U(k,\Delta\varphi) = \frac{1}{2}k\Delta\varphi^2$ denotes the potential energy storage function of a torsional spring with stiffness k and deflection $\Delta\varphi$.

Let V_{SEA} and V_{PEA} be a time varying Lyapunov candidate functions for the SEA and PEA topologies, respectively:

$$V_{\text{SEA}} = T(J_o,\dot{\tilde{\varphi}}_o) + T(J_{i,d},\dot{\tilde{\varphi}}_i) + U(k_s,\tilde{\varphi}_i - \tilde{\varphi}_o) + U(k_c,\tilde{\varphi}_i), \tag{10}$$

$$V_{\text{PEA}} = T(J_{i,d},\dot{\tilde{\varphi}}_o) + U(k_s,\tilde{\varphi}_o) + U(k_c,\tilde{\varphi}_o)\,, \tag{11}$$

which are valid candidate functions if they are positive definite. This is true for the following conditions:

$$k_s > 0\,, \quad k_c > 0\,. \tag{12}$$

The origin $\tilde{\varphi}_o = \tilde{\varphi}_i = \dot{\tilde{\varphi}}_i = \dot{\tilde{\varphi}}_o = 0$ is said to be stable for an actuator if the derivative of the candidate function is negative semi-definite and asymptotically stable if it is negative definite [36]. This also proves that the stored energy of the system does not increase and it is therefore passive. Consider, then, the corresponding time derivatives:

$$\dot{V}_{\text{SEA}} = J_o \ddot{\tilde{\varphi}}_o \dot{\tilde{\varphi}}_o + J_{i,d} \ddot{\tilde{\varphi}}_i \dot{\tilde{\varphi}}_i + k_s(\tilde{\varphi}_i - \tilde{\varphi}_o)(\dot{\tilde{\varphi}}_i - \dot{\tilde{\varphi}}_o) + k_c \tilde{\varphi}_i \dot{\tilde{\varphi}}_i\,, \tag{13}$$

$$\dot{V}_{\text{PEA}} = J_{i,d} \ddot{\tilde{\varphi}}_o \dot{\tilde{\varphi}}_o + (k_s + k_c)\tilde{\varphi}_o \dot{\tilde{\varphi}}_o\,. \tag{14}$$

Applying the closed-loop dynamic Eqs. (7) and (9) from the SEA and PEA topologies to their respective candidate function derivatives yield the following results:

$$\dot{V}_{\text{SEA}} = -d_c \dot{\tilde{\varphi}}_i^2\,, \quad \dot{V}_{\text{PEA}} = -d_c \dot{\tilde{\varphi}}_o^2\,, \tag{15}$$

which are both negative semi-definite when $d_c \geq 0$ and negative definite when $d_c > 0$. This proves that, in free motion, the controlled systems in both SEA and PEA topologies are locally stable around the trajectory, i.e., the origin $\tilde{\varphi}_o = \tilde{\varphi}_i = \dot{\tilde{\varphi}}_i = \dot{\tilde{\varphi}}_o = 0$ is a local stable equilibrium point. Furthermore, local asymptotic stability is achieved when the system is damped.

3.4. Stiffness adaptation

We consider a scenario where the elastic behavior of an actuator may vary during operation due to the occurrence of faults. The interaction stiffness, which is apparent to a human touching the output, is denoted as k_{int} and is defined by [28] as the static relation between the interaction torque τ_{int} and the output deviation $\tilde{\varphi}_o$. For SEA structures, the interaction stiffness corresponds to the series combination of k_s and k_c, while for PEA structures, it corresponds to the parallel combination:

$$k_{\text{int,SEA}} = \frac{k_s k_c}{k_s + k_c}\,, \quad k_{\text{int,PEA}} = k_s + k_c\,. \tag{16}$$

To maintain a consistent perceived interaction for the user despite variations in the actuator stiffness, we can manipulate the virtual stiffness k_c to maintain a desired level of interaction stiffness $k_{\text{int},d}$:

$$k_{c,\text{SEA}} = \frac{k_s k_{\text{int},d}}{k_s - k_{\text{int},d}}, \quad k_{c,\text{PEA}} = k_{\text{int},d} - k_s\,. \tag{17}$$

Applying the stability conditions in Eq. (12) we obtain that for the SEA the following must hold: $0 < k_{\text{int},d} < k_s$. While for the PEA the following must hold: $k_{\text{int},d} > k_s$. Hence, the interaction stiffness in a SEA can only be softer than its inherent stiffness, while in a PEA it can only be stiffer.

The adaptation law in Eq. (17), particularly for SEA structures, is a simple strategy to attain a desired steady state behavior in the output torque-deflection relationship. However, this adaptation strategy does not consider the transient behavior that can occur from the response of the fourth-degree mechanical system in Eq. (7), nor the model mismatches that might affect the overall interaction experience with the user. Yet, it might provide a level of consistency in user interaction.

4. Experimental systems

To evaluate the general control strategy and demonstrate its applicability to different actuators, we consider two actuator designs: A mechanically adjustable compliance and controllable equilibrium position actuator (MACCEPA) described in [37], which has a SEA topology with nonlinear elastic torque characteristics; and a redundantly actuated series–parallel elastic actuator (+SPEA) described in [38], which has a PEA structure with multiple parallel springs and individual adjustable equilibrium positions. For experimentation both actuators were mounted on test benches and loaded with pendulums. The general control strategy presented in Section 2 is applied to both actuators. Yet, this section details the specific dynamic characteristics and the implementation of trajectory generation and fault detection for each actuator.

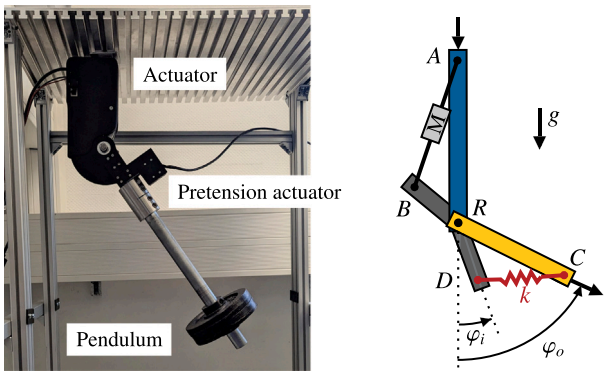

(a) (b)

Fig. 3. (a) MACCEPA experimental setup. (b) Kinematic model of the MACCEPA.

4.1. MACCEPA

The experimental setup and kinematic diagram of the actuator is shown in Fig. 3(b). It consists of an input link (*A*-*R*), an output link (*C*-*R*), and a lever arm (*B*-*R*-*D*). The input and lever arm are coupled by a motor screw drive between points *A* and *B*, while the output and lever arm are coupled by a linear spring with stiffness k between points *C* and *D*. Angular positions φ_o and φ_i are measured with absolute encoders, while the angular speeds $\dot{\varphi}_o$ and $\dot{\varphi}_i$ are determined through numerical differentiation. The actuator is torque controlled and the torque τ_i exerted at the rotation point *R* is available through force measurement using strain gauge in the screw drive [26]. The high level control of the actuator is programmed in a real-time machine using Matlab/Simulink R2019a interfaced with TwinCAT 3 from Beckhoff. Low-level control and the processing of inputs and outputs are performed on the actuator's on-board PCB, which communicates with the real-time machine via EtherCAT, with a sampling frequency of 1000 Hz. An external tensor mechanism, powered by a Dynamixel servomotor, can add up to 4.5 mm of pretension to the linear spring.

The complex kinematic configuration of the actuator, considering the linear spring connection, means that there is a nonlinear torsional elastic coupling between the motorized input and the output link. The elastic torque created by the mechanism is a nonlinear function that depends on the deflection $\alpha = \varphi_i - \varphi_o$ and pretension distance P of the linear spring [39]:

$$\mathrm{f}_{s,\text{MAC}}(\alpha) = k L_C L_D \sin\alpha \left(1 + \frac{P - |L_D - L_C|}{L_{CD}}\right), \tag{18}$$

where L_C and L_D denote the lengths of segments *C*-*R* and *D*-*R*, respectively, and $L_{CD} = \sqrt{L_C^2 + L_D^2 - 2L_C L_D \cos\alpha}$.

The instantaneous stiffness $k_{s,\text{MAC}}$ is the partial derivative of $\mathrm{f}_{s,\text{MAC}}(\alpha)$ with respect to α:

$$k_{s,\text{MAC}} = \frac{\partial \mathrm{f}_{s,\text{MAC}}}{\partial\alpha}(\alpha) = k L_C L_D \cos\alpha \left(1 + \frac{P - |L_D - L_C|}{L_{CD}}\right) - k L_C^2 L_D^2 \sin^2\alpha \left(\frac{P - |L_D - L_C|}{L_{CD}^3}\right), \tag{19}$$

which holds the stability condition in Eq. (12) for $P > 0$.

The pendulum load, with mass m, distance to its center of mass l, and gravity acceleration g, exerts a gravitational torque at the output and defines the output inertia:

$$\tau_{g,o} = mgl \sin\varphi_o\,, \quad J_o = ml^2\,. \tag{20}$$

At the output, friction does not have a significant dynamic effect and is therefore neglected, i.e., $\tau_{\text{fric},o} = 0$, while at the input, it is modeled as Coulomb and viscous friction [40]:

$$\tau_{\text{fric},i} = \mu_c \tanh(S\dot{\varphi}_i) + \mu_v \dot{\varphi}_i, \tag{21}$$

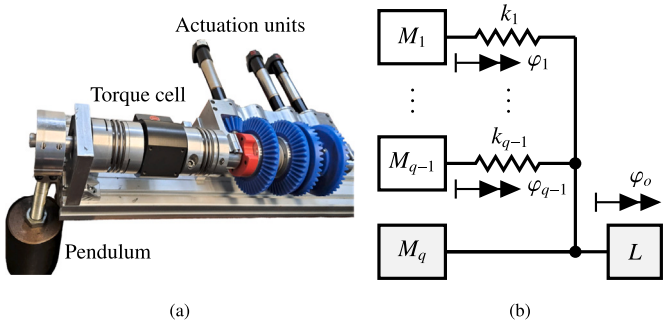

Fig. 4. (a) +SPEA experimental setup with $q = 3$ actuators. (b) Conceptual diagram of the actuator. M denotes motorized units and L denotes load.

where μ_c is the Coulomb torque coefficient, μ_v is the viscous friction coefficient, and S is a factor that shapes the transition between the velocity sign values using a tanh function.

4.2. +SPEA

The experimental system and conceptual diagram of the actuator are shown in Fig. 4. It consists of q actuation units with identical motor and transmission characteristics. One unit is rigidly coupled to the load, while $q-1$ are coupled through torsional springs with stiffness $k_1, \dots, k_{q-1}$. The positions of the elastic units are denoted as $\varphi_1, \dots, \varphi_{q-1}$, while the position of the rigid actuation unit coincides with the output φ_o. All positions are measured by incremental encoders and speeds are computed using low-passed filtered numerical derivation. The output torque τ_o is measured by a DRBK torque transducer from ETH Messtechnik connected at the output shaft. As detailed in [27], the elastic actuation units $M_1, \dots, M_{q-1}$ are position-controlled, while the rigid actuation unit M_q is current controlled. The high-level control for the actuator was developed in Matlab/Simulink R2019b on a host machine interfaced with a Speedgoat real-time target machine. Input/output modules were used to interface the Speedgoat machine with sensors and motor drivers (EPOS 4 50/5 from Maxon).

The rigid connection between the main actuation unit M_q and output, means that M_q provides torque directly to the load and is mainly responsible for its position. The elastic units $M_1, \dots, M_{q-1}$ provide additional support through the elastic deformation of their torsional springs. If we consider positions $\varphi_1, \dots, \varphi_{q-1}$ as adjustable equilibrium positions for the springs, the structure of the actuator can be considered as that of a PEA with multiple parallel springs. Thus, the control strategy is applicable with the assumption that the low-level position controllers in the elastic units are infinitely fast. The combined elastic torque provided by the multiple springs in parallel is a function of the output position and the individual positions of each unit, such as:

$$\mathrm{f}_{s,+\mathrm{SPEA}}(\varphi_o) = \sum_{j=1}^{q-1} k_j(\varphi_o - \varphi_j) = \mathbf{k}\left(\mathbf{1}\varphi_o - \boldsymbol{\Phi}\right), \tag{22}$$

where $\mathbf{k} = \begin{bmatrix} k_1 & \dots & k_{q-1} \end{bmatrix}$ and $\boldsymbol{\Phi} = \begin{bmatrix} \varphi_1 & \dots & \varphi_{q-1} \end{bmatrix}^\intercal$.

The instantaneous stiffness is the combined stiffness of the parallel springs:

$$k_{s,+\mathrm{SPEA}} = \frac{\partial \mathrm{f}_{s,+\mathrm{SPEA}}}{\partial \varphi_o}(\varphi_o) = \sum_{j=1}^{q-1} k_j . \tag{23}$$

The dynamics of the rigid actuator, loaded with a pendulum, are characterized with respect to Eq. (8) by:

$$J_i = J_m r^2 c_{\eta,o} + ml^2 , \tag{24}$$

$$\tau_{\mathrm{fric},o} = \mu_{v,m}\dot{\varphi}_o r^2 c_{\eta,o} , \tag{25}$$

$$\tau_{g,o} = mgl \sin\varphi_o , \tag{26}$$

$$\tau_i = K_M I_q r c_{\eta,o} , \tag{27}$$

where J_m and $\mu_{v,m}$ denote the motor inertia and viscous friction coefficient, respectively, K_M is the motor torque constant, I_q is the current of the rigidly connected motor, r is the transmission ratio of the gearbox, and the function $c_{\eta,o}$ captures the switching of the maximum efficiency η with respect to the flow of energy in the unit [41]:

$$c_{\eta,o} = \begin{cases} \eta & \text{if } \tau_o\dot{\varphi}_o \geq 0 \\ \frac{1}{\eta} & \text{if } \tau_o\dot{\varphi}_o < 0 \end{cases}, \tag{28}$$

$$\tau_o = \tau_{g,o} + \sum_{j=1}^{q-1} k_j(\varphi_o - \varphi_j) + \tau_{\mathrm{int}} , \tag{29}$$

The dynamics of the redundant elastic units, with index $j = 1, \dots, q-1$, are described by:

$$J_m r\ddot{\varphi}_j + B_m r\dot{\varphi}_j = K_M I_j - \frac{\tau_j}{r c_{\eta,j}} , \tag{30}$$

$$\tau_j = k_j(\varphi_j - \varphi_o) , \tag{31}$$

$$c_{\eta,j} = \begin{cases} \eta & \text{if } \tau_j\dot{\varphi}_j \geq 0 \\ \frac{1}{\eta} & \text{if } \tau_j\dot{\varphi}_j < 0 \end{cases}, \tag{32}$$

where I_j denotes the current of each motor, and $c_{\eta,j}$ captures their efficiency switch.

4.3. Trajectory generation

As explained in Section 2.2, the elastic torque can be used to compensate for output dynamics by selecting a suitable deflection reference α_d that solves Eq. (3). While we propose the same compensation torque for any elastic actuator, the method for finding a solution for $\mathrm{f}_s(\alpha_d)$ needs to consider the actuator characteristics of each experimental system.

The main challenge of planning a trajectory in both actuators is their dynamic complexity. The elastic coupling in the MACCEPA makes it necessary to compute a suitable input reference that attains the desired output trajectory, but requires numerical methods due to its nonlinear dynamic. In the +SPEA, positioning the output is easier due to the rigid connection to the main actuation unit, but a control allocation algorithm is needed to coordinate the redundant units.

4.3.1. Nonlinear torque function

Considering that elastic torque of the MACCEPA is a nonlinear function of the deflection, the solution can be found by applying the Newton–Raphson method [42] at each time step to find the root of the function $\mathrm{h}(\alpha_d) = \mathrm{f}_{s,\mathrm{MAC}}(\alpha_d) - J_o\ddot{\varphi}_{o,d} - \tau_{g,o} - \tau_{\mathrm{fric},o}$, which becomes zero when Eq. (3) is met. The method is implemented in an iterative fashion with discrete instances $n = 0, 1, 2, \dots$, as:

$$\alpha_d(n+1) = \alpha_d(n) - \frac{\mathrm{h}(\alpha_d(n))}{\mathrm{h}'(\alpha_d(n))}, \tag{33}$$

where $\mathrm{h}'(\alpha) = \frac{\partial \mathrm{f}_{s,\mathrm{MAC}}}{\partial \alpha}(\alpha)$. The method starts with an initial guess $\alpha_d(0)$ and ends when the value of $|\mathrm{h}(\alpha_d)|$ is below a threshold.

4.3.2. Control allocation for redundant units

Considering the multiple elastic units of the +SPEA, finding a set of reference positions for the elastic units $\boldsymbol{\Phi}_d$ that attains the required compensation torque can lead to infinite solutions due to the redundancy of the actuator. This can be generally solved by applying control allocation methods such as distributing the compensation torque equally among the available elastic units. However, this might lead to over-deflections in the springs in cases of high stiffness degradation [27]. In this work, we consider a method which aims to find the least-squares solution for deflection:

$$\boldsymbol{\Phi}_d = \mathbf{1}\varphi_{o,d} - \mathbf{k}^\dagger\left(J_o\ddot{\varphi}_{o,d} + \tau_{g,o} + \tau_{\mathrm{fric},o}\right). \tag{34}$$

By using the pseudoinverse of the stiffness vector $\mathbf{k}^\dagger$, the method in Eq. (34) finds the reference which leads to the least squared combined deflection for the parallel springs.

4.4. Fault detection

We consider stiffness faults as deviations in the expected elastic behavior of the actuator. In order to detect such faults, we implement observers based on the Kalman filter algorithm that monitor the pertinent parameters that determine the elastic torque function. The Kalman filter generally requires a discrete model, with discrete time instances t_n and $n = 0, 1, 2, \dots$, which is defined for a single-input multiple-output (SIMO) as:

$$\mathbf{x}_{n+1} = \mathbf{F}(\mathbf{x}_n, u_n) + \mathbf{w}_n, \tag{35}$$

$$\mathbf{y}_{n+1} = \mathbf{H}(\mathbf{x}_n, u_n) + \mathbf{v}_n, \tag{36}$$

where $\mathbf{x}_n$ includes system states, u_n denotes the measured or known input, and $\mathbf{y}_n$ includes output measurements. The system model is defined by the function $\mathbf{F}(\mathbf{x}_n, u_n)$ and process noise $\mathbf{w}_n$, while the observation model is defined by function $\mathbf{H}(\mathbf{x}_n, u_n)$ and measurement noise $\mathbf{v}_n$. The Kalman filter algorithm initially performs a prediction step using the discrete model and later corrects the prediction using the available output measurements (measurement update). Two Kalman filter algorithms were implemented in this work: the unscented Kalman filter (UKF) and the extended Kalman filter (EKF). These two algorithms differ mainly in their formulation and the manner in which the Gaussian random variable is propagated through the system dynamics [43] but both are widely used in state and parameter estimation algorithms for nonlinear systems. Particularly, the UKF was used in the MACCEPA due to its higher nonlinearity, while the EKF was better suited for the +SPEA motor units where the only source of nonlinearity is the efficiency function.

4.4.1. Unscented Kalman filter for MACCEPA

In the MACCEPA, faults could particularly occur in the cable that connects the spring to the output side. Damages in the cable threads, for example, could lower the spring pretension. For our experimentation, we modify and estimate the value of pretension, using a UKF design, to emulate and detect such faults. The method could equally be utilized to estimate other changing parameters, e.g., the spring stiffness k.

We include the pretension as state, the deflection measurement as input, and the elastic torque as measured output:

$$\mathbf{x}_n = \left[P(t_n)\right], \tag{37}$$

$$u_n = \alpha(t_n), \tag{38}$$

$$\mathbf{y}_n = \left[\tau_s(t_n)\right]. \tag{39}$$

The elastic torque τ_s is indirectly measured by knowing the input torque τ_i which is determined from measuring the force at the base of the motor in the MACCEPA and calculating the torque at the rotation point through the transmission of the gearbox and screw drive [44]. The torque τ_s is then estimated considering Eq. (6b), by removing the friction component and neglecting inertia:

$$\tau_s(t_n) = \tau_i(t_n) - \mu_c \tanh(S\dot{\varphi}_i(t_n)) - \mu_v \dot{\varphi}_i(t_n). \tag{40}$$

The system and observation models are defined as:

$$\mathbf{F}(\mathbf{x}_n, u_n) = \mathbf{x}_n, \tag{41}$$

$$\mathbf{H}(\mathbf{x}_n, u_n) = \left[kL_C L_D \sin\left(\alpha(t_n)\right) \left(1 + \frac{P(t_n) - |L_D - L_C|}{\sqrt{L_C^2 + L_D^2 - 2L_C L_D \cos\left(\alpha(t_n)\right)}} \right) \right] \tag{42}$$

The UKF algorithm is detailed in [43]. The output of the filter is the estimated state vector:

$$\hat{\mathbf{x}} = \left[\hat{P}\right]. \tag{43}$$

The estimated pretension value $\hat{P}$ is then fed back to the calculations of trajectory generation and impedance control, while the estimated stiffness value is used for calculation of the exact stiffness adaptation:

$$\hat{k}_{s,\mathrm{MAC}}(t_n) = kL_C L_D \cos\left(\alpha(t_n)\right) \left(1 + \frac{\hat{P}(t_n) - |L_D - L_C|}{L_{CD,n}} \right) - kL_C^2 L_D^2 \sin^2\left(\alpha(t_n)\right) \left(\frac{\hat{P}(t_n) - |L_D - L_C|}{L_{CD,n}^3} \right), \tag{44}$$

where $L_{CD,n} = \sqrt{L_C^2 + L_D^2 - 2L_C L_D \cos\left(\alpha(t_n)\right)}$.

The UKF algorithm from [43] was implemented considering additive (zero mean) noise. The algorithm includes tunable parameters set to $\alpha = 0.001$, $\kappa = 0$, and $\beta = 2$, according to the author's suggestion. The measurement covariance matrix $\mathbf{R}$, corresponding to the noise covariance of the torque measurement, was set to $\mathbf{R} = [0.7]$. While the state noise covariance matrix $\mathbf{Q}$, was tuned to $\mathbf{Q} = [1 \times 10^{-10}]$.

4.4.2. Extended Kalman filter for +SPEA

In the +SPEA, we consider stiffness degradation faults for springs $k_1, \dots, k_{q-1}$. To detect such faults we implement individual observers using an EKF design that consider the actuation-side dynamics described in Eq. (30).

The discrete model consists of the following input, state vector and output measurement vector (denoted with index $j = 1, \dots, q-1$):

$$u_n = I_j(t_n), \tag{45}$$

$$\mathbf{x}_n = \begin{bmatrix} \varphi_o(t_n) & \varphi_j(t_n) & \dot{\varphi}_j(t_n) & k_j(t_n) \end{bmatrix}^{\mathsf{T}}, \tag{46}$$

$$\mathbf{y}_n = \begin{bmatrix} \varphi_o(t_n) & \varphi_j(t_n) \end{bmatrix}^{\mathsf{T}}. \tag{47}$$

The system and observation models are then defined as:

$$\mathbf{F}(\mathbf{x}_n, u_n) = \mathbf{x}_n + \Delta t\, \dot{\mathbf{x}}_n, \tag{48}$$

$$\mathbf{H}(\mathbf{x}_n, u_n) = \begin{bmatrix} 1 & 0 & 0 & 0 \\ 0 & 1 & 0 & 0 \end{bmatrix} \mathbf{x}_n, \tag{49}$$

where Δt is the time step and the system updates are captured by:

$$\dot{\mathbf{x}}_n = \begin{bmatrix} 0 \\ \dot{\varphi}_j \\ \frac{K_M}{rJ_m} I_j - \frac{B_m}{J_m}\dot{\varphi}_j - \frac{k_j(\varphi_j - \varphi_o)}{J_m r^2 c_{\eta,j}} \\ 0 \end{bmatrix}_{t_n}. \tag{50}$$

The EKF algorithm from [45] is then applied to obtain an estimated state vector $\hat{\mathbf{x}} = \begin{bmatrix} \hat{\varphi}_o & \hat{\varphi}_j & \hat{\dot{\varphi}}_j & \hat{k}_j \end{bmatrix}^{\mathsf{T}}$. The state and measurement noise covariance matrices were set to $\mathbf{Q} = \mathrm{diag}\left(1 \times 10^{-9}, 1 \times 10^{-9}, 1 \times 10^{-9}, 5 \times 10^{-11}\right)$ and $\mathbf{R} = \mathrm{diag}\left(1 \times 10^{-6}, 1 \times 10^{-6}\right)$. The estimated stiffness values $\hat{k}_j$ were then fed back to the calculations of trajectory generation, impedance control, and exact stiffness adaptation.

5. Evaluation

To evaluate the control strategy, output trajectory tracking experiments were conducted in faulty conditions and under interaction disturbance with both experimental systems shown in Figs. 3(a) and 4(a). Additionally, interaction experiments were also carried out in the MACCEPA to evaluate the capability of the strategy to modulate the output stiffness and detect faults during continuous interaction with a lever.

In the MACCEPA, faults were emulated by lowering the spring pretension P through the external tensor mechanism. The external servomotor receives angular target positions which are mapped to desired pretension values. As mentioned in Section 4.4.1, changes in pretension emulate faults in the kinematic elements that connect the spring to the actuator links. In our experiments, we emulated intensive and sudden changes in pretension to showcase the applicability of the control method in an actuator with nonlinear characteristics.

In the +SPEA, each elastic coupling is equipped with four parallel custom laser-cut spiral springs. During an experiment, we emulated a sudden degradation of the spring stiffness k_1 by disengaging one of its four spiral springs from the output shaft, effectively lowering the

Table 1
Parameters of the MACCEPA.

Description		Value
Input-side inertia	J_i	1.9×10^{-4} kg m^2
Spring stiffness	k	118.3×10^3 N m^{-1}
Lever arm segment length	L_C	0.056 m
Output link length	L_D	0.0645 m
Mass of pendulum	m	7 kg
Length of pendulum	l	0.40 m
Gravitational acceleration	g	9.81 m s^{-2}
Input viscous fric. coeff.	μ_v	0.2

stiffness approximately 25%, by pulling it with a cable. This emulated a failure in the fixation or a sudden deformation in the springs.

External disturbance torque τ_{int} was introduced by interacting directly with the pendulum. The value of the interaction torque was then estimated offline from output dynamics.

5.1. Trajectory tracking with nonlinear actuator

For experimentation with the MACCEPA we considered two trajectory references: an oscillatory function with a frequency of 0.2 Hz, and a sigmoid function that showcases the advantage of direct torque sensing for estimation in static conditions.

For trajectory tracking without continuous disturbance, the control parameters can be freely selected without affecting the tracking performance. To maintain the stability condition in Eq. (12) and keep a stiff control setting, the interaction stiffness was set to $k_{\text{int},d} = 50$ N m rad^{-1} and the pretension was kept above 1 mm. The virtual damping was set to $d_c = 2$ N m s rad^{-1} and no inertia shaping was active, i.e., $J_{i,d} = J_i$. The list of relevant actuator parameters is shown in Table 1. Dimension parameters were taken from [37], the input inertia was identified in [26] for an actuator of the same design, and the friction parameters for the actuator used in this work were identified experimentally with the Parameter Estimator application from Simulink using measurements from the actuator under oscillatory pendulum loading and the model in Eq. (6b). The estimation was carried out with Matlab R2022b (AMD Ryzen™ 5 4500U, 2.38 GHz, 16.0 GB RAM), using the nonlinear least squares method with the Levenberg–Marquardt algorithm.

5.1.1. Fault compensation

Fig. 5 shows results for an oscillatory trajectory tracking experiment without interaction. Faults were emulated at times $t = 33$ s and $t = 68$ s, marked in the plots with gray dash-dotted lines, by lowering the pretension from 3.8 mm to 2.8 mm and then to 1.7 mm. The experiment started with the actuator and pendulum positions at the origin, i.e., $\varphi_i = \varphi_o = 0°$, and an initial estimated pretension $\hat{P}(0) = 0$ N m rad^{-1}, which made the system deviate from the reference trajectory and deflection at the beginning of the experiment. The reference trajectory was promptly tracked as the pretension estimation converged to the reference value. After each fault occured, the pretension was correctly estimated using the UKF observer and the amplitude of the deflection $\varphi_i - \varphi_o$ increased to compensate for the lower pretension value, all while tracking the output trajectory accurately. Small oscillatory deviations occurred in the estimated pretension, which might be due to model mismatches and/or sensor errors.

5.1.2. Emulated interaction

Fig. 6 shows results for an oscillatory trajectory tracking experiment with interaction occurring at times $t = 16$ s, $t = 28$ s, $t = 76$ s, and $t = 83$ s, marked in the plots with dotted lines. A fault was emulated at time $t = 46$ s, marked in the plots with a dash-dotted line, by lowering the pretension from 3.7 mm to 2.5 mm. The output deviation $\tilde{\varphi}_o$, shown in the plots, make it clear that the trajectory was accurately tracked in normal conditions. When interaction disturbance occurred,

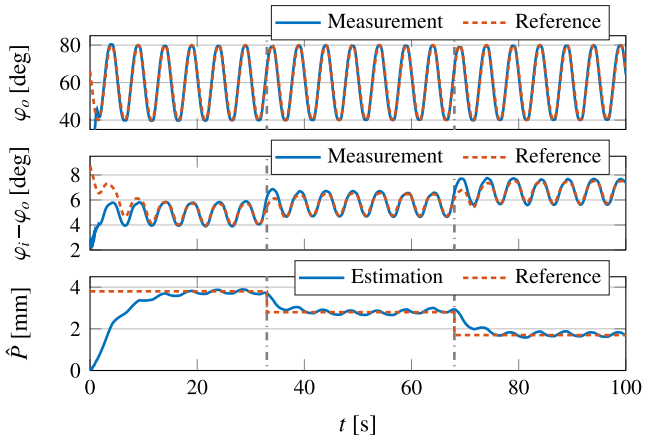

Fig. 5. Results of MACCEPA oscillatory trajectory tracking with emulated faults (marked by gray dash-dotted lines) and no interaction. The observed pretension showed oscillatory behavior but it was accurately estimated. The output trajectory was accurately tracked and faults were compensated through increased deformation amplitude.

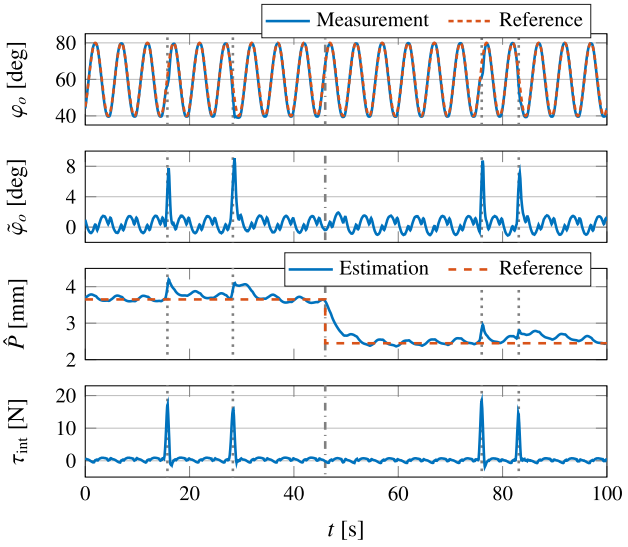

Fig. 6. Results of MACCEPA oscillatory trajectory tracking with interactions (marked by gray dotted lines) and emulated fault (gray dash-dotted line). The output trajectory was accurately tracked when no interaction was present. While under interaction disturbance, the trajectory and estimation deviated from the reference values but returned to their correct values once the disturbance was removed.

the trajectory and the estimation deviated from their references, but were promptly corrected once the interaction was removed.

Fig. 7 shows results for a sigmoid trajectory tracking experiment with interaction occurring at times $t = 43$ s, $t = 49$ s, $t = 101$ s, and $t = 105$ s, marked in the plots by dotted lines. A fault was emulated at time $t = 79$ s by lowering the pretension from 2.8 mm to 2.1 mm. The experiment started at $\varphi_o = 30°$ and with the pretension already converged to its reference value. Notice that, as the actuator moved to the position $\varphi_o = 60°$, the estimated pretension deviated from its reference, similarly to the case of oscillatory trajectory, but promptly corrected itself. Furthermore, similar to the oscillatory tracking experiments, the output trajectory was accurately tracked since the fault was compensated by increasing the amplitude of the deflection as the stiffness got softer. The interaction torque caused disturbances in the system that affected the tracked trajectory and estimation, but both were corrected after the disturbance was removed.

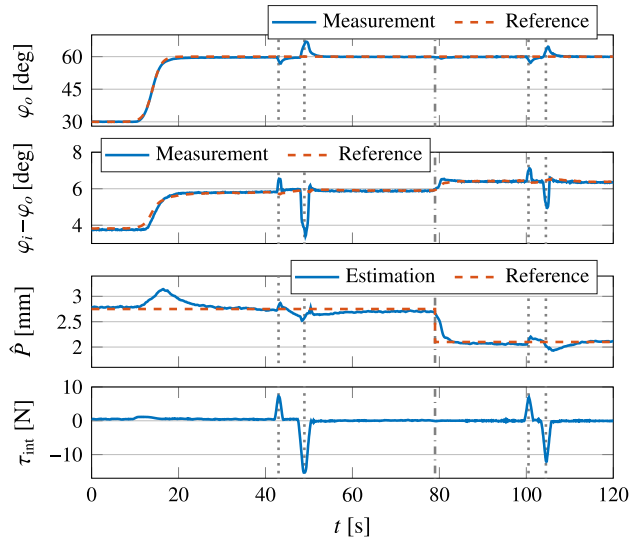

Fig. 7. Results of MACCEPA sigmoid trajectory tracking with interactions (marked by gray dotted lines) and an emulated fault (marked by gray dash-dotted line). The output trajectory was accurately tracked and the fault was correctly compensated. Under interaction disturbance, the trajectory and estimation deviated from their references but returned to their correct values once the disturbance was removed.

Table 2
Parameters of the +SPEA.

Description		Value
Motor+transmission inertia	J_m	3.37×10^{-6} kg m^2
Viscous friction coefficient	B_m	6.66×10^{-6} N m s rad^{-1}
Motor torque constant	K_M	0.0136 N m A^{-1}
Transmission reduction ratio	r	353
Max. transmission efficiency	η	0.64
Mass of the pendulum	m	6 kg
Distance to center of mass	l	0.26 m
Gravitational acceleration	g	9.81 m s^{-2}

5.2. Trajectory tracking with redundant actuator

Similarly to the MACCEPA, for experimentation with the +SPEA we considered scenarios of oscillatory motion with a frequency of 0.2 Hz that demonstrate the potential of the actuator to dynamically adjust the equilibrium position of multiple parallel springs for dynamic load compensation. The actuator was equipped with $q = 3$ units, one of which was directly coupled to a pendulum output and two were coupled elastically. The couplings for the elastic units, comprised of the 4 parallel custom laser-cut spiral springs, should achieve a stiffness of 8.4 N m rad^{-1} according to [38]. However, during experimentation, the stiffness estimations converged at $\hat{k}_1 = 7.4$ N m rad^{-1} and $\hat{k}_2 = 7.8$ N m rad^{-1}. A stiffness fault was emulated by disengaging one of the four spiral springs of k_1, effectively lowering its stiffness approximately 25%. For accurate trajectory tracking and high interaction disturbance rejection, the interaction stiffness was set to $k_{\text{int},d} = 100$ N m rad^{-1}. The virtual damping was set to $d_c = 1$ N m s rad^{-1} and no inertia shaping was active, i.e., $J_{i,d} = J_i$. The list of parameters for the +SPEA, taken from [46], is shown in Table 2.

5.2.1. Fault compensation

Fig. 8 shows the results of an oscillatory reference tracking without interaction. A fault was emulated at time $t = 45$ s, marked in the plots by a gray dash-dotted line. The estimation of $\tilde{k}_1$ and $\tilde{k}_2$ using the EKF algorithm both started at their converged values. After the fault occurred, the observed stiffness $\hat{k}_1$ lowered approximately 22% of its original value: $\hat{k}_1 = 5.8$ N m rad^{-1}, which is consistent with disengaging one of the four spiral springs that comprise the elastic coupling. Similar

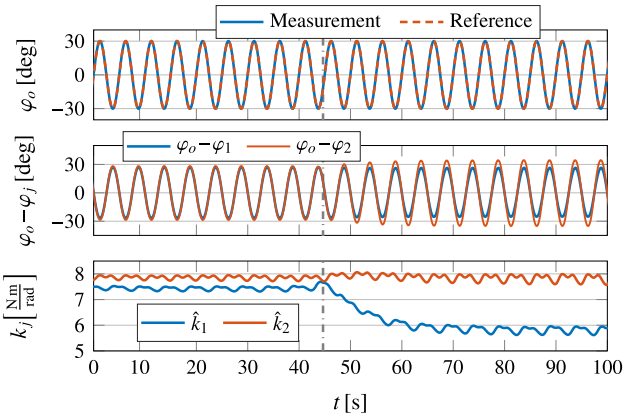

Fig. 8. Results of +SPEA oscillatory reference tracking without interactions and fault emulation (marked by gray dash-dotted line) in unit 1. The estimated stiffness presented oscillatory behavior but coincided with expected values. The output trajectory was accurately tracked. The trajectory of both elastic units were affected by fault occurrence to compensate for output dynamics.

to the experiments with the MACCEPA, the estimation in the +SPEA during oscillatory motion showed an oscillatory behavior but it did not seem to reduce the performance of the controller, which achieved an accurate trajectory tracking. The trajectory generation algorithm modified the positions of both elastic units after the fault occurred to minimize overall deflection, which made it necessary for the system to increase the deflection of unit 2, which remained stiffer, to compensate for the faulty one.

5.2.2. Emulated interaction

Fig. 9 shows the results of an oscillatory reference tracking with interactions occurring at times $t = 10$ s, $t = 41$ s, and $t = 104$ s, marked in the plots by gray dotted lines, and a fault was emulated at time $t = 73$ s, marked in the plot by a gray dash-dotted line. Similarly to the results of the MACCEPA experiments, the output trajectory was accurately tracked under normal and faulty conditions and it deviated under interaction disturbance. The stiffness estimation performed equally well as in the previous experiment.

5.3. Stiffness modulation with nonlinear actuator

While the previous experiments showed that the control strategy is capable of attaining accurate trajectory tracking in the face of faulty conditions and interaction disturbance, an important advantage of this controller is its ability to modulate the interaction behavior. In other words, to vary the amount of output deviation $\tilde{\varphi}_o$ that is allowed with respect to the interaction torque τ_{int}. In static conditions, or for sufficiently low frequencies, the expected interaction behavior is $\tau_{\text{int}} = k_{\text{int}} \tilde{\varphi}_o$. This makes the stiffness adaptation, described in Section 3.4, useful to modulate the interaction despite changes in the inherent stiffness, e.g., due to nonlinearity or faults. However, this approximation generally requires high model accuracy, particularly concerning friction, which is critical in actuators where the friction is complex and difficult to model accurately. This is the case, for example, in the MACCEPA, where there are multiple friction components due to the different stages in the transmission, from the motor shaft, through the geared screw-drive, and finally the rotating lever arm. While the friction torque was approximated to a Coulomb and viscous friction model, as described in Eq. (21), the actual friction behavior might vary due to lubrication or wear, and some unidentified friction components might remain uncompensated.

Previous research showed that stiffness adaptation can be made more robust to friction model mismatches by increasing the virtual

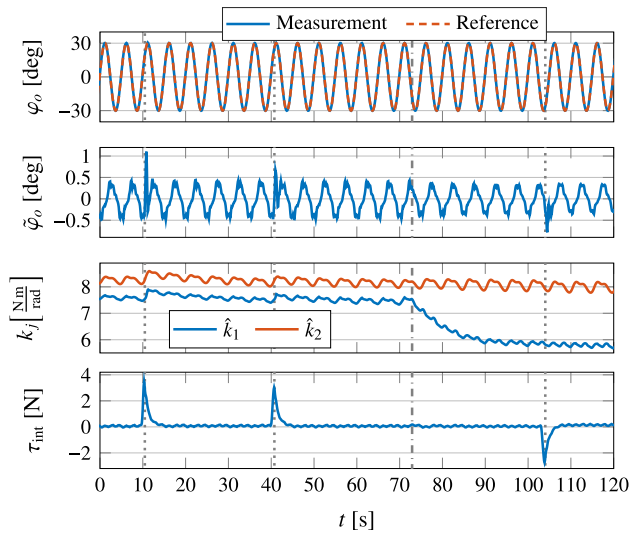

Fig. 9. Results of +SPEA oscillatory reference tracking with interaction disturbance (marked by gray dotted lines) and an emulated fault (marked by a gray dash-dotted line). The output trajectory was accurately tracked when no interaction was present. While under interaction disturbance, the trajectory and estimation deviated from the reference values but returned to their correct values once the disturbance was removed.

Fig. 10. Experimental setup for interaction experiment. A fixed reference position of 30° is set, and the user interacts by moving the lever up and down at a fixed pace, trying to exert the same force throughout the experiment.

stiffness or adding inertia shaping [47]. Therefore, inertia shaping might be beneficial to maintain robustness in low-stiffness settings.

To evaluate the ability of the control strategy to modulate the interaction stiffness in the MACCEPA with and without inertia shaping, we conducted an experiment where a user interacted directly with the actuator through a lever. The experimental setup is shown in Fig. 10. The lever was aligned such that, at $\varphi_o = 0°$, it is perpendicular to the direction of gravity, making the gravitational component:

$$\tau_{g,o} = mgl \cos \varphi_o \,, \tag{51}$$

with $m = 1.8\,\text{kg}$, $l = 0.2\,\text{m}$.

During experimentation, a fixed reference position of $\varphi_{o,d} = 30°$ was set for the lever, which serves as the equilibrium interaction position. The user was instructed to perform an oscillatory motion moving the lever up and down at a fixed pace of $0.4\,\text{Hz}$, guided by an auditory metronome. No specific position limits were requested, but the user was instructed to try to exert the same amount of force to the lever during the whole interaction. The virtual stiffness for control of the MACCEPA was set to $d_c = 0\,\text{N m s rad}^{-1}$, while two interaction stiffnesses were considered: $k_{\text{int}} = 20\,\text{N m rad}^{-1}$ and $k_{\text{int}} = 50\,\text{N m rad}^{-1}$. Furthermore, inertia shaping was inactive when setting the desired inertia to the real input inertia, i.e., $J_{i,d} = J_i$, and active by setting the desired inertia to half of the input inertia, i.e., $J_{i,d} = 0.5 J_i$.

Fig. 11 shows the result of experiments with $k_{\text{int}} = 20\,\text{N m rad}^{-1}$ with and without inertia shaping. The plots show the position of the lever and the actuator deflection, measured through encoders. A fault was emulated at $t = 15\,\text{s}$ by lowering the pretension from $3.5\,\text{mm}$ to $1.8\,\text{mm}$. The pretension estimations showed some disturbance to the interaction torque, but correctly oscillated around the reference values, showing that fault detection using the UKF algorithm was successful under continuous interaction. Finally, the interaction torque was estimated offline based on the output dynamics from Eq. (6a) and compared to the expected interaction behavior $\tau_{\text{int}} = k_{\text{int}} \tilde{\varphi}_o$. Note that, without inertia shaping, the interaction torque deviated from the expected behavior. This deviation seems to be pronounced when approaching zero speed in the negative direction, which might suggest an unmodeled direction-dependent Stribeck friction component. With inertia shaping, on the other hand, the expected interaction torque behavior was more accurately attained, showing the advantage of inertia shaping to improve the robustness of the method.

Fig. 12 shows the result of experiments with $k_{\text{int}} = 50\,\text{N m rad}^{-1}$ with and without inertia shaping. As with the previous experiments, the plots show the position of the lever and the actuator deflection, measured through encoders. A fault was emulated at $t = 15\,\text{s}$ by lowering the pretension from $3.5\,\text{mm}$ to $1.8\,\text{mm}$. The pretension estimations again oscillated around the correct reference values under continuous interaction. The interaction torque, estimated offline, is compared to the expected interaction behavior $\tau_{\text{int}} = k_{\text{int}} \tilde{\varphi}_o$. Note that, the same way as with the previous experiment, the interaction torque deviated from the expected behavior without inertia shaping. The deviation, however, was not as pronounced as with the lower stiffness setting, showing that a higher virtual stiffness improves the robustness. Finally, the expected interaction torque was better attained when inertia shaping was active, showing again the ability of the control strategy to accurately modulate the interaction behavior.

5.4. Discussion

Experimental results demonstrated the versatile applicability of the control strategy for different actuator designs. The accuracy of the controller is evident throughout the trajectory tracking experiments. In essence, the control law in Eq. (2) is that of a PD position controller with feedback and feedforward compensations. Combined with a trajectory generation algorithm that compensates for output dynamics, the control strategy achieves accurate tracking performance when no disturbance is present, and deviates from the output trajectory under user interaction, according to the selected interaction stiffness. The strategy is then improved by considering faulty conditions, which are specific to the particular actuator design. The ability of the strategy to adapt the interaction stiffness behavior is made evident through experiments with a lever, which showed that virtually reducing the actuator inertia can help make the method more robust to model mismatches.

Relying on the reconfiguration of the control law to achieve desired output dynamics, the proposed strategy in this article can be compared to the Model Reference Adaptive Control (MRAC) approach which aims at updating the control parameters to obtain a desired reference closed-loop dynamic model [48]. In literature, MRAC approaches are proposed to handle uncertain parameters in elastic actuators [33,34]. Calanca et al.[33] proposed a MRAC for linear SEAs which relied on online estimation of human interaction dynamic parameters for robust torque control. Rather than modeling human interaction, the passivity-based impedance controller in our approach directly regulates the relationship between torque and position at the output. Losey et al. [34] proposed a modified MRAC for torque control of linear series-elastic actuators (SEA) which translates the torque requirement into a position

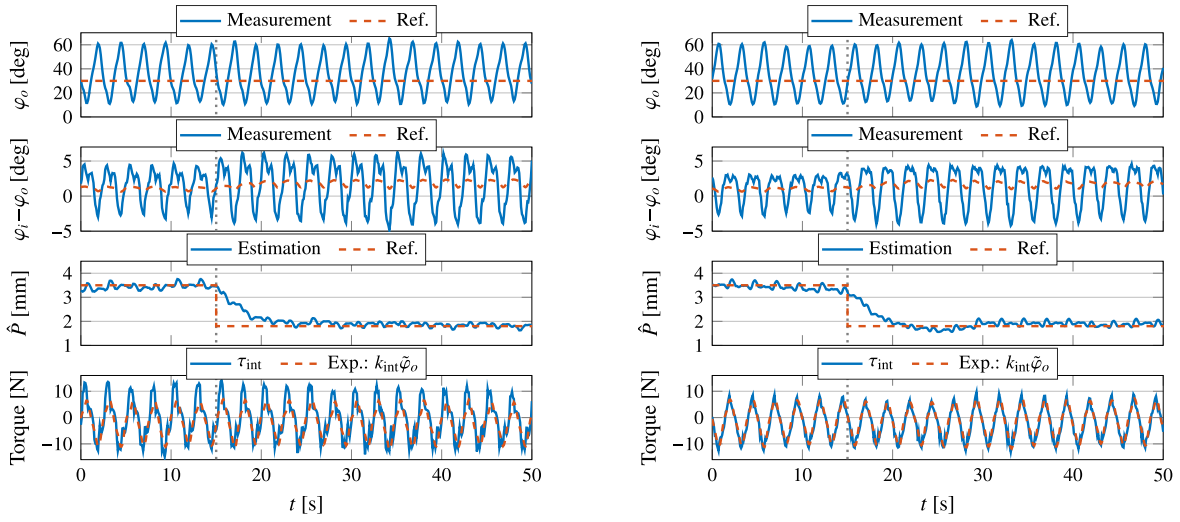

(a) $J_{i,d} = J_1$ (No inertia shaping)

(b) $J_{i,d} = 0.5J_i$ (Shaped inertia)

Fig. 11. Results of interaction experiments using MACCEPA with $k_{\text{int}} = 20\,\text{N m rad}^{-1}$ and with inertia shaping (a) inactive and (b) active. Interaction torque was added by moving the lever up and down at a pace of 0.4 Hz. The pretension estimations oscillated around the correct reference values under continuous interaction and emulated faults (marked by gray dash-dotted lines). The interaction torque was compared to the expected behavior $\tau_{\text{int}} = k_{\text{int}}\tilde{\varphi}_o$. Without inertia shaping, the interaction torque deviated from the expected behavior, possibly due to unmodeled friction components. Inertia shaping improved the robustness of the control strategy, attaining the expected interaction behavior more accurately.

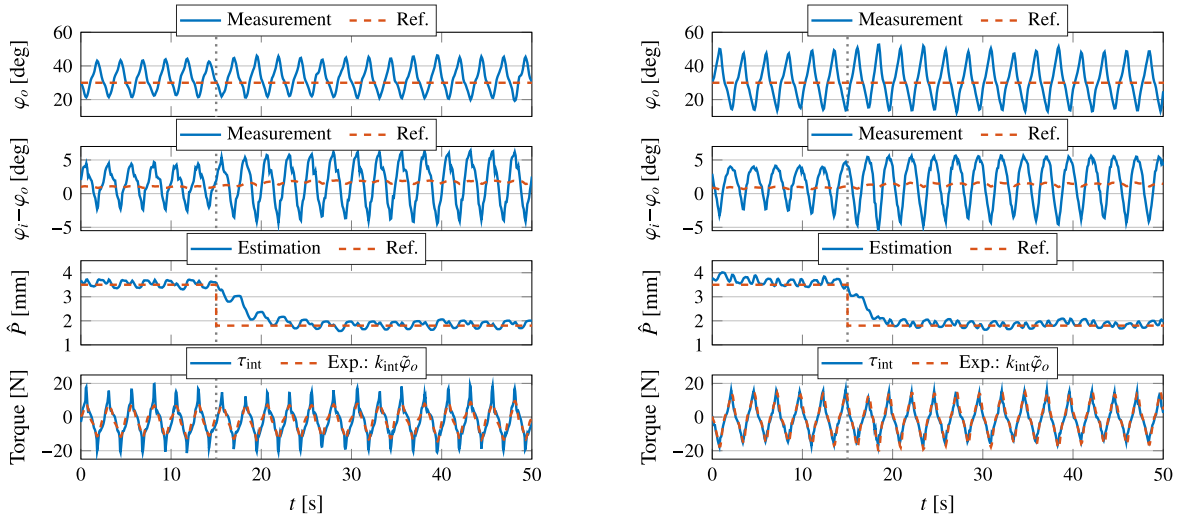

(a) $J_{i,d} = J_1$ (No inertia shaping)

(b) $J_{i,d} = 0.5J_i$ (Shaped inertia)

Fig. 12. Results of interaction experiments using MACCEPA with $k_{\text{int}} = 50\,\text{N m rad}^{-1}$ and with inertia shaping (a) inactive and (b) active. Interaction torque was added by moving the lever up and down at a pace of 0.4 Hz. The pretension estimations oscillated around the correct reference values under continuous interaction and emulated faults (marked by gray dash-dotted lines). The interaction torque was compared to the expected behavior $\tau_{\text{int}} = k_{\text{int}}\tilde{\varphi}_o$. Without inertia shaping, the interaction torque deviated from the expected behavior, but remained close due to the higher virtual stiffness setting. Inertia shaping improved the robustness of the control strategy, attaining the expected interaction behavior more accurately.

reference with the use of passivity-based impedance control and adapts the closed-loop dynamics based on online estimation of the system's inertia, damping, stiffness and Coulomb friction, making the strategy robust to parameter changes. Their strategy is similar to our approach in that it takes advantage of an adaptive impedance control and online parameter estimation to obtain a desired output impedance model. They reported similarly accurate tracking performance in a SEA, while implementing online parameter identification to determine unknown quantities. In this article, we performed online parameter estimation with the purpose of detecting stiffness faults. The small deviations found in the parameter estimation under dynamic conditions, which might be caused by model mismatches and/or sensor errors, did not reduce the accuracy of the controller significantly. In a way, the fault detection algorithm could act similar to a disturbance observer that corrects any unwanted or unknown behavior in the control algorithm, and adds robustness to the control strategy.

Moreover, the strategy proposed in this article was shown to be applicable to multiple elastic actuator topologies. While SEAs are more common in literature [17], parallel elastic actuators (PEA) have also been found to have advantages in wearable robot systems due to

its potential for lower torque requirement and better position accuracy [49], and the addition of virtual compliance through control could improve safety by minimizing impact forces in a typically rigidly coupled actuator.

6. Conclusions

This article presents a stiffness-fault-tolerant control strategy for output trajectory tracking in elastic actuators. A passivity-based impedance control and a stiffness adaptation law regulate the interaction impedance behavior despite the occurrence of stiffness faults. The proposed method serves as a general trajectory tracking control design for elastic actuators which can be adapted to generate suitable reference trajectories for internal coordinates and observe relevant parameters for fault detection.

The strategy was demonstrated experimentally on two different actuation systems: a mechanically adjustable compliance and controllable equilibrium position actuator (MACCEPA), and a redundant series–parallel elastic actuator (+SPEA). With the MACCEPA we showed that strategy can effectively handle nonlinear stiffness characteristics. With the +SPEA we showed that mechanical redundancy can be exploited to further reduce the torque requirement of the main actuation unit and improve its life span. Combined with analytical redundancy through fault-tolerant control, its reliability can be further improved. Experiments with the two actuators demonstrated the applicability of the control strategy under dynamic motion and for holding static positions, and validate the strategy as a general model-based approach for adaptive compliance actuation in physical human–robot interaction (pHRI) applications.

Future work should investigate control performance for close human–robot interaction, e.g., in a wearable robot. The method could also be extended to multiple degrees of freedom and complex kinematic structures, such as underactuated soft robotic manipulators with active and passive elastic joints. Regarding redundant actuators, trajectory optimization methods considering constraints and economic costs require further examination. Finally, we expect the methods presented in this article to increase the reliability of elastic actuation systems and improve user experience in pHRI applications.

CRediT authorship contribution statement

Rodrigo J. Velasco-Guillen: Writing – review & editing, Writing – original draft, Visualization, Validation, Software, Project administration, Methodology, Investigation, Formal analysis, Data curation, Conceptualization. **Raphaël Furnémont:** Writing – review & editing, Validation, Supervision, Software, Resources. **Tom Verstraten:** Writing – review & editing, Validation, Supervision, Resources. **Bram Vanderborght:** Writing – review & editing, Validation. **Josep M. Font-Llagunes:** Writing – review & editing, Validation, Methodology. **Philipp Beckerle:** Writing – review & editing, Validation, Supervision, Resources, Project administration, Methodology, Funding acquisition, Conceptualization.

Declaration of competing interest

The authors declare that they have no known competing financial interests or personal relationships that could have appeared to influence the work reported in this paper.

Acknowledgments

This work was supported by the Deutsche Forschungsgemeinschaft (DFG) Research Grant (no. BE 5729/1) and European Cooperation in Science and Technology (COST) Action CA16116.

Data availability

Data will be made available on request.

References

[1] Blanke M, Kinnaert M, Lunze J, Staroswiecki M. Diagnosis and fault-tolerant control, third ed.. Springer; 2016.
[2] Filippini R, Sen S, Bicchi A. Toward soft robots you can depend on. IEEE Robot Autom Mag 2008;15(3):31–41.
[3] Jiang Y, Hu Q, Ma G. Adaptive backstepping fault-tolerant control for flexible spacecraft with unknown bounded disturbances and actuator failures. ISA Trans 2010;49(1):57–69.
[4] Song Q, Song Y-D. Data-based fault-tolerant control of high-speed trains with traction/braking notch nonlinearities and actuator failures. IEEE Trans Neural Netw 2011;22(12):2250–61.
[5] Gao X, Zhang J-X, Hao L. Fault-tolerant control of pneumatic continuum manipulators under actuator faults. IEEE Trans Ind Inf 2021;17(12):8299–307.
[6] Mokhtari M, Taghizadeh M, Ghaf-Ghanbari P. Adaptive second-order sliding model-based fault-tolerant control of a lower-limb exoskeleton subject to tracking the desired trajectories augmented by CPG algorithm. J Braz Soc Mech Sci Eng 2022;44(9):423.
[7] Rong Y, Chou W, Jiao R. Robust fault-tolerant motion/force control of a fully-actuated hexarotor using adaptive sliding mode impedance control. Internat J Robust Nonlinear Control 2022;32(7):4149–72.
[8] Hogan N. Impedance control: An approach to manipulation. In: 1984 American control conference. IEEE; 1984, p. 304–13.
[9] Rocon E, Ruiz A, Raya R, Schiele A, Pons JL, Belda-Lois J, Poveda R, Vivas M, Moreno J. Human-robot physical interaction. Wearable Robots Biomech Exoskeletons 2008;127–63.
[10] He W, Ge SS, Li Y, Chew E, Ng YS. Impedance control of a rehabilitation robot for interactive training. In: Social robotics: 4th international conference, ICSR 2012, Chengdu, China, October 29-31, 2012, Proceedings. Springer; 2012, p. 526–35.
[11] Sharifi M, Azimi V, Mushahwar VK, Tavakoli M. Impedance learning-based adaptive control for human–robot interaction. IEEE Trans Control Syst Technol 2021;30(4):1345–58.
[12] Mokhtari M, Taghizadeh M, Mazare M. Impedance control based on optimal adaptive high order super twisting sliding mode for a 7-DOF lower limb exoskeleton. Meccanica 2021;56:535–48.
[13] Foroutannia A, Akbarzadeh-T M-R, Akbarzadeh A, Tahamipour-Z SM. Adaptive fuzzy impedance control of exoskeleton robots with electromyography-based convolutional neural networks for human intended trajectory estimation. Mechatronics 2023;91:102952.
[14] Verstraten T, Beckerle P, Furnémont R, Mathijssen G, Vanderborght B, Lefeber D. Series and parallel elastic actuation: Impact of natural dynamics on power and energy consumption. Mech Mach Theory 2016;102:232–46.
[15] Beckerle P, Verstraten T, Mathijssen G, Furnemont R, Vanderborght B, Lefeber D. Series and parallel elastic actuation: Influence of operating positions on design and control. IEEE/ASME Trans Mechatronics 2017;22(1):521–9.
[16] Mathijssen G, Lefeber D, Vanderborght B. Variable recruitment of parallel elastic elements: Series–parallel elastic actuators (SPEA) with dephased mutilated gears. IEEE/ASME Trans Mechatronics 2014;20(2):594–602.
[17] Vanderborght B, Albu-Schaeffer A, Bicchi A, Burdet E, Caldwell D, Carloni R, Catalano M, Eiberger O, Friedl W, Ganesh G, Garabini M, Grebenstein M, Grioli G, Haddadin S, Hoppner H, Jafari A, Laffranchi M, Lefeber D, Petit F, Stramigioli S, Tsagarakis N, Damme MV, Ham RV, Visser L, Wolf S. Variable impedance actuators: A review. Robot Auton Syst 2013;61(12):1601–14.
[18] Beckerle P. Practical relevance of faults, diagnosis methods, and tolerance measures in elastically actuated robots. Control Eng Pract 2016;50:95–100.
[19] Lemaitre J, Dufailly J. Damage measurements. Eng Fract Mech 1987;28(5):643–61.
[20] Isermann R. Fault-diagnosis applications: model-based condition monitoring: actuators, drives, machinery, plants, sensors, and fault-tolerant systems. Springer; 2011.
[21] Flacco F, De Luca A. Stiffness estimation and nonlinear control of robots with variable stiffness actuation. IFAC Proc Vol 2011;44(1):6872–9, 18th IFAC World Congress.
[22] Flacco F, De Luca A, Sardellitti I, Tsagarakis NG. On-line estimation of variable stiffness in flexible robot joints. Int J Robot Res 2012;31(13):1556–77.
[23] Menard T, Grioli G, Bicchi A. A stiffness estimator for agonistic-antagonistic variable-stiffness-actuator devices. IEEE Trans Robot 2014;30(5):1269–78.
[24] Liu Z, Jin H, Liu Y, Zhao J. An online stiffness estimation approach for variable stiffness actuators using lever mechanism. IEEE Robot Autom Lett 2022;7(3):6709–17.

[25] Stuhlenmiller F, Velasco-Guillen RJ, Rinderknecht S, Beckerle P. Fault-tolerant physical human-robot interaction via stiffness adaptation of elastic actuators. In: Human-friendly robotics 2019: 12th international workshop. Springer; 2020, p. 73–87.
[26] Velasco-Guillen RJ, Grosu V, Vanderborght B, Font-Llagunes JM, Beckerle P. Experimental evaluation of a stiffness-fault-tolerant control strategy on an elastic actuator for wearable robotics. In: 2022 9th IEEE RAS/EMBS international conference for biomedical robotics and biomechatronics (BioRob). IEEE; 2022, p. 1–6.
[27] Velasco-Guillen RJ, Furnémont R, Verstraten T, Beckerle P. A stiffness-fault-tolerant control strategy for a redundant elastic actuator. In: 2022 IEEE/ASME international conference on advanced intelligent mechatronics. AIM, IEEE; 2022, p. 1360–5.
[28] Ott C. Cartesian impedance control of redundant and flexible-joint robots. Springer; 2008.
[29] Wang M, Sun L, Yin W, Dong S, Liu J. Continuous robust control for series elastic actuator with unknown payload parameters and external disturbances. IEEE/CAA J Autom Sin 2017;4(4):620–7.
[30] Lanh LAK, Duong VT, Nguyen HH, Kim SB, Nguyen TT. Hybrid adaptive control for series elastic actuator of humanoid robot. Int J Intell Unmanned Syst 2023;11(3):359–77.
[31] Oh S, Kong K. High-precision robust force control of a series elastic actuator. IEEE/ASME Trans Mechatronics 2017;22(1):71–80.
[32] Asignacion A, Haninger K, Oh S, Lee H. High-stiffness control of series elastic actuators using a noise reduction disturbance observer. IEEE Trans Ind Electron 2022;69(8):8212–9.
[33] Calanca A, Fiorini P. Human-adaptive control of series elastic actuators. Robotica 2014;32(8):1301–16.
[34] Losey DP, Erwin A, McDonald CG, Sergi F, O'Malley MK. A time-domain approach to control of series elastic actuators: Adaptive torque and passivity-based impedance control. IEEE/ASME Trans Mechatronics 2016;21(4):2085–96.
[35] Narayan J, Abbas M, Dwivedy SK. Robust adaptive backstepping control for a lower-limb exoskeleton system with model uncertainties and external disturbances. Automatika 2023;64(1):145–61.
[36] Khalil H. Nonlinear Systems. Pearson education, third ed.. Prentice Hall; 2002.
[37] Ducastel V, Langlois K, Rossini M, Grosu V, Vanderborght B, Lefeber D, Verstraten T, Geeroms J. SMARCOS: Off-the-shelf smart compliant actuators for human-robot applications. Actuators 2021;10(11):289.
[38] Mathijssen G, Furnémont R, Verstraten T, Brackx B, Premec J, Jiménez R, Lefeber D, Vanderborght B. +SPEA introduction: Drastic actuator energy requirement reduction by symbiosis of parallel motors, springs and locking mechanisms. In: 2016 IEEE international conference on robotics and automation. ICRA, IEEE; 2016, p. 676–81.
[39] Bacek T, Moltedo M, Rodriguez-Guerrero C, Geeroms J, Vanderborght B, Lefeber D. Design and evaluation of a torque-controllable knee joint actuator with adjustable series compliance and parallel elasticity. Mech Mach Theory 2018;130:71–85.
[40] Andersson S, Söderberg A, Björklund S. Friction models for sliding dry, boundary and mixed lubricated contacts. Tribol Int 2007;40(4):580–7.
[41] Verstraten T, Mathijssen G, Furnémont R, Vanderborght B, Lefeber D. Modeling and design of geared DC motors for energy efficiency: Comparison between theory and experiments. Mechatronics 2015;30:198–213.
[42] Lee ET, Wang JW. Newton-raphson method. In: Statistical methods for survival data analysis. John Wiley & Sons, Ltd; 2003, p. 428–32.
[43] Wan EA, van der Merwe R. The unscented Kalman filter. Kalman Filter Neural Netw 2001;221–80.
[44] Velasco-Guillen RJ, Grosu V, Carmona-Ortiz VA, Vanderborght B, Lefeber D, Font-Llagunes JM, Beckerle P. A stiffness-fault-tolerant control strategy for an elastically actuated powered knee orthosis. In: 2020 8th IEEE RAS/EMBS international conference for biomedical robotics and biomechatronics (BioRob). IEEE; 2020, p. 660–5.
[45] Charles K. Chui GC. Kalman Filtering with Real-Time Applications. fifth ed.. Springer; 2017.
[46] Furnémont R, Mathijssen G, Verstraten T, Jimenez-Fabian R, Lefeber D, Vanderborght B. Novel control strategy for the +SPEA: a redundant actuator with reconfigurable parallel elements. Mechatronics 2018;53:28–38.
[47] Velasco-Guillen RJ, Schofer F, Bliek A, Beckerle P. Exploring the just noticeable interaction stiffness differences of an impedance-controlled series elastic actuator. Actuators 2023;12(10):378.
[48] Isidro IA, Pais DAM, Alves PM, Carrondo MJT. Online control strategies. In: Comprehensive Biotechnology. third ed.. Oxford: Pergamon; 2019, p. 943–51.
[49] Toxiri S, Calanca A, Ortiz J, Fiorini P, Caldwell DG. A parallel-elastic actuator for a torque-controlled back-support exoskeleton. IEEE Robot Autom Lett 2017;3(1):492–9.

Rodrigo J. Velasco-Guillen received his Bachelor's degree in Mechatronic Engineering from Universidad Don Bosco (El Salvador) in 2014, after which he worked as an Electrical Design Engineer at Siemens El Salvador (2014–2016). He obtained his Master's degree in Robotics and Automation at TU Dortmund in 2018 and started his doctoral candidacy in 2019 at TU Dortmund in the Elastic Lightweight Robotics group. He is currently a doctoral candidate at the chair of Autonomous Systems and Mechatronics at FAU Erlangen-Nürnberg since 2021. His research interests include human–robot interaction, elastic actuation, fault-tolerant control, and wearable robotics.

Raphaël Furnémont received the degree in study of Mechanical Engineering at the Vrije Universiteit Brussel (VUB) and Université Libre de Bruxelles (ULB) in 2013. He is a postdoctoral researcher at the Robotics and Multibody Mechanics research group. His research topics include compliant actuation, energy-efficient actuation and optimal control (ERC grant SPEAR).

Tom Verstraten is a professor at the Robotics & Multibody Mechanics Research Group (R&MM) of the Vrije Universiteit Brussel (Belgium). He worked as a visiting researcher at TU Darmstadt (Germany) in 2017, and was awarded a Fulbright grant for visiting scholars for a research stay at the University of Tulsa (United States) in 2018-19. His main research focus is the study and development of energy-efficient actuation systems for robotic prostheses, exoskeletons and collaborative robots.

Bram Vanderborght obtained his Ph.D. from the Vrije Universiteit Brussel in 2007. He performed research at JRL lab in AIST, Tsukuba (Japan) and did his post-doc researcher at the Italian Institute of Technology. Since 2009 he is professor at the VUB. He had an ERC starting grant and is currently coordinating three EU projects on smart and self healing materials for soft robots. His research interests are human–robot collaboration for applications for health and manufacturing like exoskeletons, prostheses, social robots, drones and cobots. He is affiliated to the Interuniversity Microelectronics Institute (IMEC), Belgium, as scientific collaborator.

Josep M. Font-Llagunes is Full Professor of Mechanical Engineering at Universitat Polit‘ ecnica de Catalunya (UPC). He is currently the Director of the UPC Doctoral School and the Biomechanical Engineering Lab (BIOMEC). He also co-founded the company ABLE Human Motion, which develops exoskeleton technology for people with mobility impairments. Prof. Font-Llagunes' lab develops computational methods for human movement analysis, innovative robotic exoskeletons for gait assistance, and wearable monitoring technology for rehabilitation. He has published more than 50 articles in indexed journals, 130 conference papers, and has supervised 9 Ph.D. theses. He is Editorial Board member of the journal Multibody System Dynamics.

Philipp Beckerle received his Dr.-Ing. in mechatronics from TU Darmstadt, Germany, in 2014 and his habilitation from TU Dortmund, Germany, in 2021. He is full professor and chair of Autonomous Systems and Mechatronics at FAU Erlangen-Nürnberg (www.asm.tf.fau.de) and was visiting researcher at Vrije Universiteit Brussel, Arizona State University, and University of Siena. His research interest is in human-centered mechatronics and robotics and his work was honored with various awards.